Supporting Information

Hyun-Sik Kim[a,b,c], Nicholas A. Heinz[b,1], Zachary M. Gibbs[d], Yinglu Tang[a,b,2], Stephen D. Kang[a,b]

and G. Jeffrey Snyder[a,b,3]

[a]Department of Materials Science and Engineering, Northwestern University, Evanston, Illinois 60208, USA.
[b]Materials Science, California Institute of Technology, Pasadena, California 91125, USA.
[c]Materials Research Center, Samsung Advanced Institute of Technology, Samsung Electronics, Suwon 443-803, South Korea.
[d]Division of Chemistry and Chemical Engineering, California Institute of Technology, Pasadena, California 91125, USA.

S1. Determination of the liquidus (*LC*) and solidus compositions (*SC*)

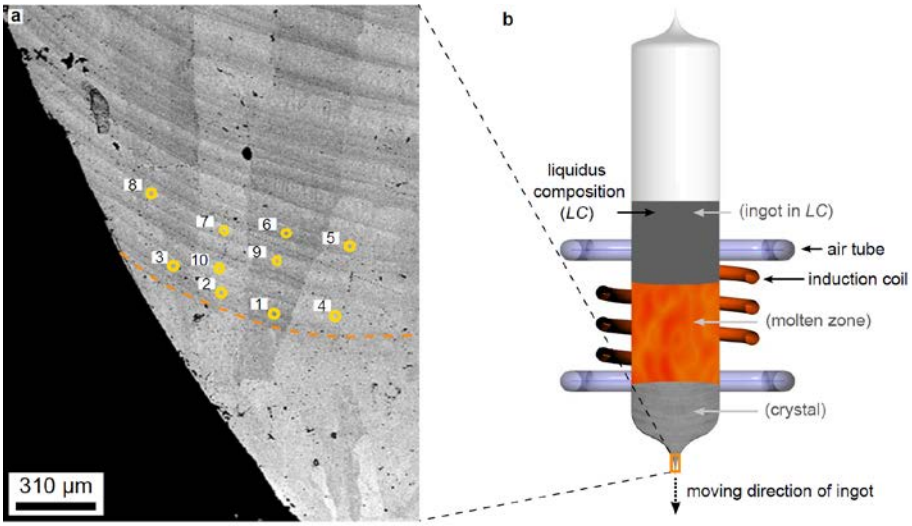

Fig. S1. Determination of liquidus compositions (*LC*) and their corresponding solidus compositions (*SC*). (*A*) Electron probe microanalysis (EPMA) on the *LC* of Bi : Sb : Te = 10.45 : 28.38 : 61.17 in at. % (see Table S1, sample "3.57E19" and "3.29E19"). Yellow circles and numbers indicate locations of composition measurements and the order of the measurements, respectively. Orange dotted line shows where texturing of the zone-melted crystal begins. This part of the crystal is from the tip of the zone-melted crystal as schematically represented in a cross-sectional view of the ingot being zone-melted (*B*).

The liquidus compositions (*LC*) and their corresponding solidus compositions (*SC*) were determined by an iterative process. For example, as a candidate for *LC*, an ingot with a composition of Bi : Sb : Te = 10.45 : 28.38 : 61.17 (in at. %) was zone-melted as in Fig. S1*B*. Unlike in Fig. 2*A* (main text), only one ingot (of *LC*) is used which results in the zone-melted crystal with a concentration gradient along the height of the crystal. Therefore, in order to accurately measure the freezing composition of the melted *LC*, electron probe microanalysis (EPMA) was done on the region where the molten zone was first solidified (orange square in Fig. S1*B*). The orange dotted line in Fig. S1*A* clearly defines the boundary between the textured crystal (curved layers) and the crystal without homogeneous orientation (below the line). Since the start of the textured crystal corresponds to that of the molten zone, EPMA measurements from ten different spots (yellow circles in Fig. S1*A*) were taken from above the orange dotted line (but still close to the line). Those spots were deliberately chosen to be closer to the surface of the crystal as the cooling air (via air tube in Fig. S1*B*) first froze the melted ingot near the surface. According to the EPMA, the averaged (from ten data points) content ratio of Sb to Bi was 0.76 ($\pm$ 0.06) (when Bi content was set to 0.25 for clarity) and the averaged Te was 60.55 at. %. As the freezing composition had an excess Te content (> 60.0 at. %) while keeping the content ratio of Bi to Sb as 0.25 : 0.75 (expressed as $(Bi_{0.25}Sb_{0.75})_2Te_{3+\delta}$) the composition of Bi : Sb : Te = 10.45 : 28.38 : 61.17 (in at. %) and its freezing composition were adopted as *LC* and *SC*, respectively. This combination of *LC* and *SC* was used in the samples "3.57E19" and "3.29E19" as listed in Table 1 (main text) and Table S1 below. After the sample "3.29E19" was synthesized, the same synthesis procedure was repeated to make "3.57E19" from the very beginning for a brief reproducibility test. All the *LC* used in Table 1 of main text, their freezing compositions estimated by EPMA

[1]Current address: Analytical Chemistry and Materials Group, Jet Propulsion Laboratory, Pasadena CA 91109.
[2]Current address: Empa, Swiss Federal Laboratories for Materials Science and Technology, Laboratory Materials for Energy Conversion, 8600 Dübendorf, Switzerland.
[3]To whom correspondence should be addressed. E-mail: jeff.snyder@northwestern.edu / Telephone number: (626) 395-6220

are given in Table S1. For *SC* of the sample "4.57E19", lower limit of the estimated Te (at. %) from the freezing composition was used.

Table S1 Freezing composition of each *LC* measured by EPMA.

Sample†	*LC*			freezing composition‡		*SC*		
	Bi (at. %)	Sb (at. %)	Te (at. %)	Bi : Sb	Te (at. %)	Bi (at. %)	Sb (at. %)	Te (at. %)
4.57E19	10.30	28.10	61.60	0.25 : 0.74 (±0.05)	60.30 (±0.17)	9.97	29.90	60.13
3.61E19	10.30	28.10	61.60	0.25 : 0.74 (±0.05)	60.30 (±0.17)	9.92	29.78	60.30
3.57E19 3.29E19	10.45	28.38	61.17	0.25 : 0.76 (±0.06)	60.55 (±0.14)	9.862	29.58	60.55
2.64E19	10.46	27.92	61.61	0.25 : 0.79 (±0.03)	61.16 (±0.54)	9.71	29.12	61.17

† Sample name = n_H of the resulting zone-levelled crystal at 300 K
‡ freezing composition = composition that melted *LC* ingots freeze into

S2. Thermoelectric transport properties

The transport properties of the zone-levelled samples of $(Bi_{0.25}Sb_{0.75})_2Te_{3+\delta}$ at 300 K including Hall carrier concentration and Hall mobility (μ_H) are given in Table S2. Each sample was named with its Hall carrier concentration value (n_H) at 300 K (Table 1 in main text).

Table S2 Transport properties of zone-levelled $(Bi_{0.25}Sb_{0.75})2Te_{3+\delta}$ at 300 K.

Sample†	n_H (cm^{-3})	S (μV/K)	σ (S/cm)	μ_H (cm^2/Vs)	κ (W/mK)	zT
6.73E19	6.73E19	142.6	2334	216.3	2.20	0.65
4.57E19	4.57E19	180.8	1515	207.0	1.89	0.79
3.61E19	3.61E19	158.8	1667	288.4	1.90	0.66
3.57E19	3.57E19	162.4	2280	399.0	1.96	0.92
3.29E19	3.29E19	156.8	2450	464.9	1.88	0.96
2.64E19	2.64E19	180.6	1885	444.9	1.76	1.05

† Sample name = n_H of the resulting zone-levelled crystal at 300 K.

S3. Two-band transport model

A two-band (TB) model was employed to compute transport properties of the zone-levelled $(Bi_{0.25}Sb_{0.75})_2Te_{3+\delta}$ samples at 300 K. For each nonparabolic band, Boltzmann transport equations (as functions of chemical potential) were numerically solved (in Python) to obtain chemical potential dependent thermoelectric parameters (i.e. Seebeck coefficient, carrier concentration, mobility, Hall coefficient, and Lorenz number.) while assuming acoustic phonon scattering[1] and alloy scattering[2] (no alloy scattering for Bi_2Te_3 and Sb_2Te_3). The resulting transport properties from the two valence bands (VB_1 and VB_2 in Fig. 1 of main text) were calculated by taking conductivity-weighted averages of the thermoelectric parameters of each band[3].

The energy gap between the lowest conduction band (*CB*) and the highest valence band for $0 \le x \le 0.75$ (VB_1) used in the TB model was taken from Sehr *et al.*[4] (Fig. 1 of main text and $\Delta E_{CB\text{-}VB1}$ in Fig. S3*A*). For $x > 0.75$, the $\Delta E_{CB\text{-}VB1}$ (green in Fig. S3*A*) was linearly extrapolated to minimize complexity. In order to determine the energy gap ($\Delta E_{CB\text{-}VB2}$) between the *CB* and the second highest valence band (VB_2), the density-of-states effective mass (m^*) and deformation potential (E_{def}) for each valence band at $x = 0$ and $x = 1$ were first tentatively fitted to experimental data from the literature while adjusting $\Delta E_{CB\text{-}VB2}$ (purple in Fig. S3*A*) at $x = 0$ and 1. We chose to start the fitting from $x = 0$ (Bi_2T_3) and $x = 1$ (Sb_2Te_3) because we did not have to consider the alloy scattering at these compositions and there were many experimental literature data points available for more accurate fitting (as in Figs. S4*A*, S4*B*, S6*C*, and S6d). Our analysis is consistent with the two valence bands are crossing at $x = 0.75$: $\Delta E_{CB\text{-}VB2}$ at $x = 0.75$ is the same as the $\Delta E_{CB\text{-}VB1}$ at x = 0.75 (from Sehr *et al.*[4]). It was found that the $\Delta E_{CB\text{-}VB2}$ at $x = 0.75$ and the fitted $\Delta E_{CB\text{-}VB2}$ at $x = 0$ and 1 could be joined in a straight (with small deviations). For simplicity, the $\Delta E_{CB\text{-}VB2}$ was assumed to change linearly with the composition (x), and the

$\Delta E_{CB\text{-}VB2}$ for other x were obtained from the straight line joining the $\Delta E_{CB\text{-}VB2}$ at x = 0.75 and that at x = 0 (for x = 1, their m^* and E_{def} were refitted with the updated $\Delta E_{CB\text{-}VB2}$ at x = 1, which was then on top of the line joining the $\Delta E_{CB\text{-}VB2}$ at x = 0.75 and 0). For 0.75 < x ≤ 1, the highest valence band is the VB_2 and the $\Delta E_{CB\text{-}VB2}$ serves as the energy gap (between the lowest CB and the highest valence band). The fitted energy gap at x = 1 used in the TB model (0.2007 eV of $\Delta E_{CB\text{-}VB2}$ in Fig. 3S*A*) is about 16 % smaller than degeneracy-corrected optical energy gap from Sehr *et al.*[4] (reasonable given the tendency to overestimate the optical energy gap as degeneracy increases)[5].

Based on the band structure information ($\Delta E_{CB\text{-}VB1}$ and $\Delta E_{CB\text{-}VB2}$ shown in Fig. 3S*A*) obtained from the literature and the fitting to the experimental literature data of x = 0 and 1, the m^* and E_{def} of each band for 0 < x < 1 were also fitted to the experimental literature data (for x = 0.75, the zone-levelled $(Bi_{0.25}Sb_{0.75})_2Te_{3+\delta}$ samples were also included). As shown in Figs. 3S*B* and 3S*C*, both the m^* and E_{def} varied linearly with the composition x. For Bi_2Te_3-Sb_2Te_3 alloys (0 < x < 1), a reduction of carrier mobility due to electron scattering from atomic disorder (the same disorder that decreases the lattice thermal conductivity from point defect scattering) was taken into account in the TB model. As the mobility is related to the total relaxation time, the total relaxation time used for 0 < x < 1 was calculated by Matthiessen's rule: $\tau_{total}^{-1} = \tau_{ac}^{-1} + \tau_{alloy}^{-1}$, where τ_{ac} and τ_{alloy} were the relaxation times for acoustic phonon scattering and alloy scattering, respectively. In the τ_{alloy} equation (from Wang *et al.*[2]) used in the TB model, there was a free parameter U that determined the magnitude of the electron scattering from alloy disorder. A constant U of 0.35 eV was used for all x.

Anisotropy of the bands was also considered in the TB model. Stordeur *et al.*[6] have optically measured effective masses along longitudinal ($m_{||}^*$) and transverse ($m_{\perp}^*$) ellipsoid directions. However, since Stordeur *et al.* assumed that only a single band was participating in transport only composition-dependent $m_{||}^*$ and $m_{\perp}^*$ for a single valence band was available. Hence, in the TB model the $m_{||}^*/m_{\perp}^*$ = 2.29 (Stordeur *et al.* reported this value for x = 0.75) was assumed for both valence bands and for all x to minimize the complexity.

The elastic constants ($C_l = d \times v_l^2$ where d and v_l are the density and the longitudinal sound velocity, respectively) of Bi_2Te_3 (x = 0) and Sb_2Te_3 (x = 1) were calculated from the d and v_l of x = 0 (d = 7700 kg/m^3 and v_l = 2143 m/s from ref. [7, 8]) and x = 1 (d = 6500 kg/m^3 and v_l = 2333 m/s from ref. [7, 8]). The C_l for the rest x were linearly interpolated between those of x = 0 and 1 (Fig. S3*D*).

As shown in Figs. S4, S5, and S6, band parameters used in the TB model (Fig. S3) yielded satisfactory fits to the experimental literature data at 300 K. The underlying physics of the measured transport properties in $(Bi_{1-x}Sb_x)_2Te_3$ single/oriented crystals is satisfactorily captured in the fits provided by the TB model. The linearly changing band parameters (with respect to the composition x) determined from the TB model and the satisfactory fit of the TB model to the experimental data strongly confirm that the band convergence at x = 0.75.

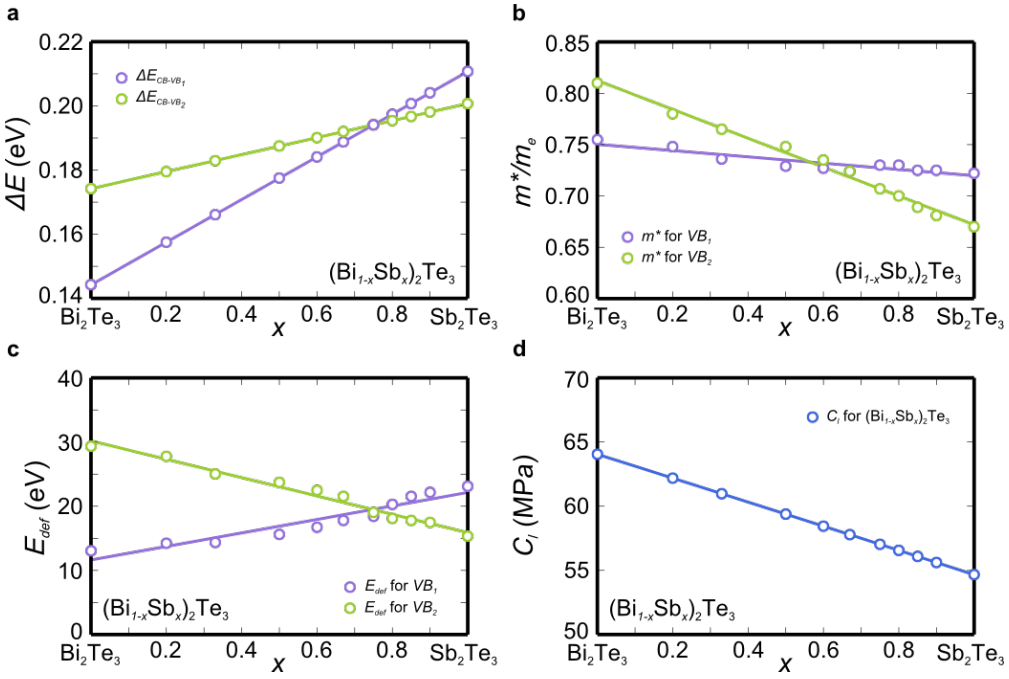

Fig. S3. Composition-dependent band parameters used in the TB model. The energy gap (ΔE) between the lowest conduction band and each valence band (*A*), the density-of-states effective mass (m^*) (*B*), deformation potential (E_{def}) (*C*) for each valence, and the elastic constant (C_l) (*D*) are given. The empty circles are the values used in the TB model for x = 0, 0.2, 0.33, 0.5, 0.6, 0.67, 0.77, 0.8, 0.85, 0.9, and 1. The solid lines are guide to the eye.

S4. Single Parabolic Band (SPB) model and Two-Band (TB) model of $(Bi_{1-x}Sb_x)_2Te_3$ for $0 \le x \le 1$

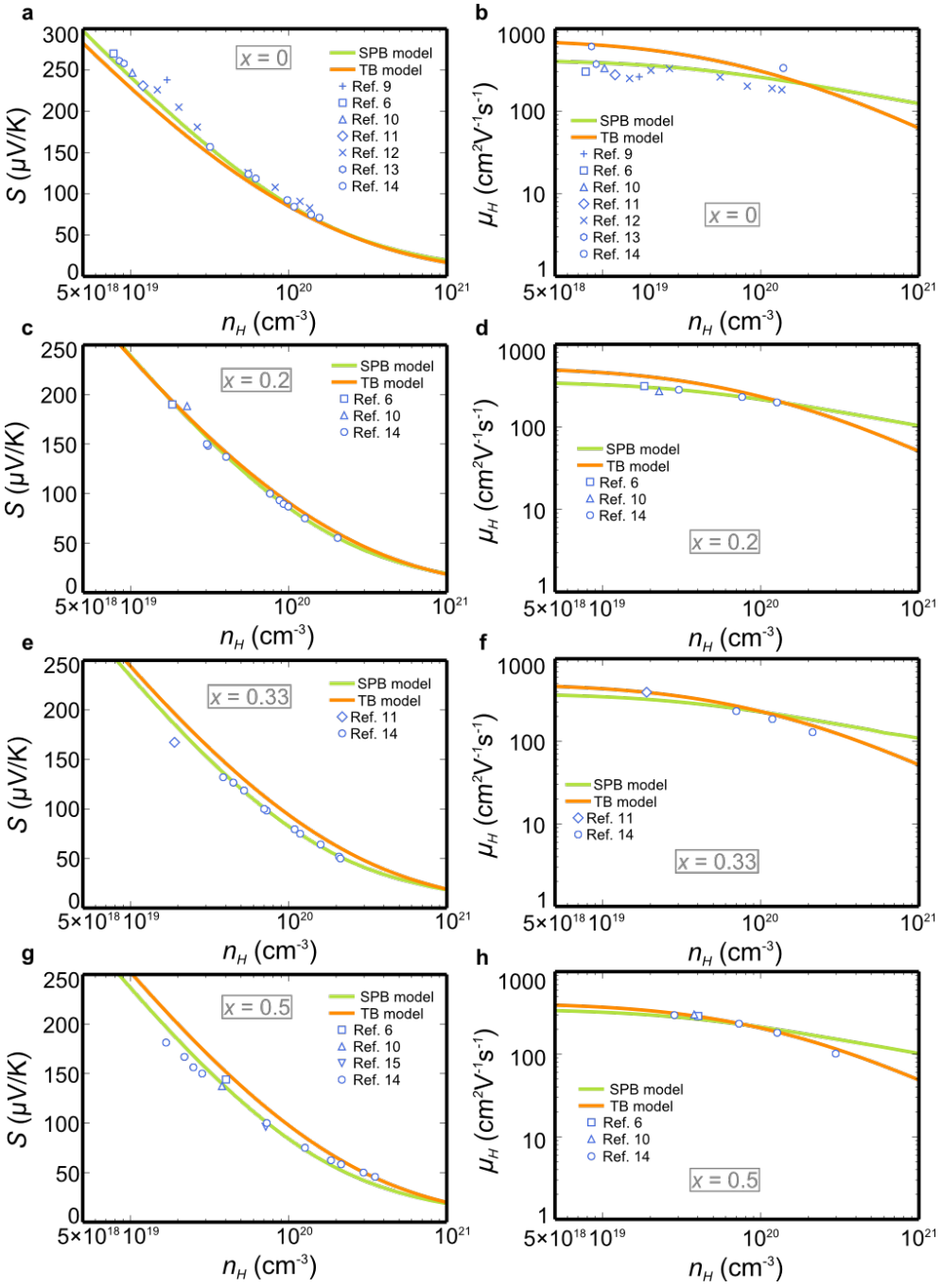

Fig. S4. Transport properties as a function of Hall carrier concentration (n_H) for $(Bi_{1-x}Sb_x)_2Te_3$ at 300 K. The Seebeck coefficient (S) and Hall mobility (μ_H) calculated by the TB model for x = 0 (*A*, *B*), 0.2 (*C*, *D*), 0.33 (*E*, *F*), and x = 0.5 (*G*, *H*) are shown in orange lines. The TB model was fitted to the literature data from Ref. [6, 9-13], and Ref. [14] (empty shapes in blue). The result of SPB model (green line) was also plotted for comparison.

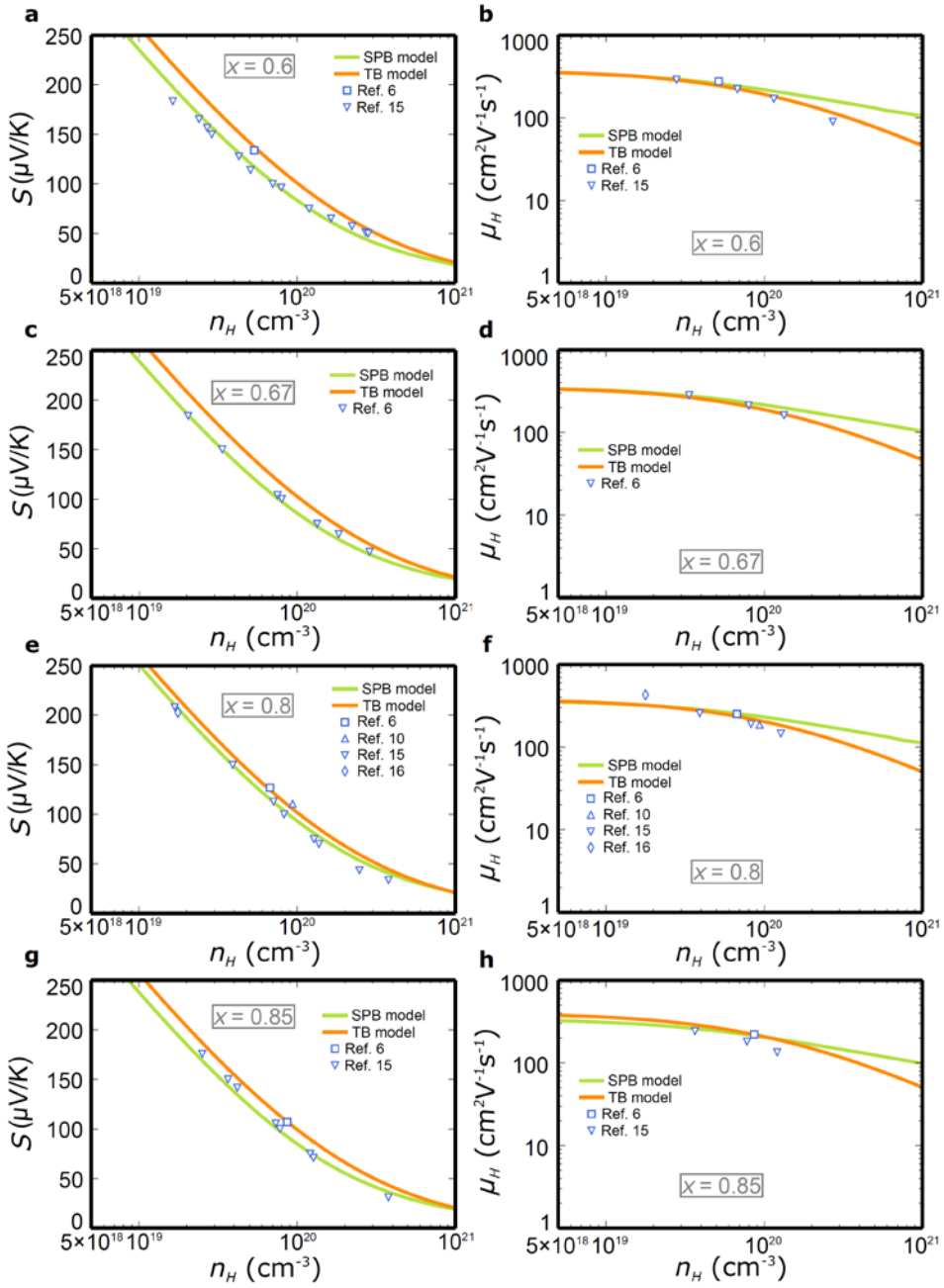

Fig. S5. Transport properties as a function of Hall carrier concentration (n_H) for $(Bi_{1-x}Sb_x)_2Te_3$ at 300 K. The Seebeck coefficient (S) and Hall mobility (μ_H) calculated by the TB model for x = 0.6 (*A*, *B*), 0.67 (*C*, *D*), 0.8 (*E*, *F*), and x = 0.85 (*G*, *H*) are shown in orange lines. The TB model was fitted to the literature data from Ref. [6, 10, 15], and Ref. [16](empty shapes in blue). The result of SPB model (green line) was also plotted for comparison.

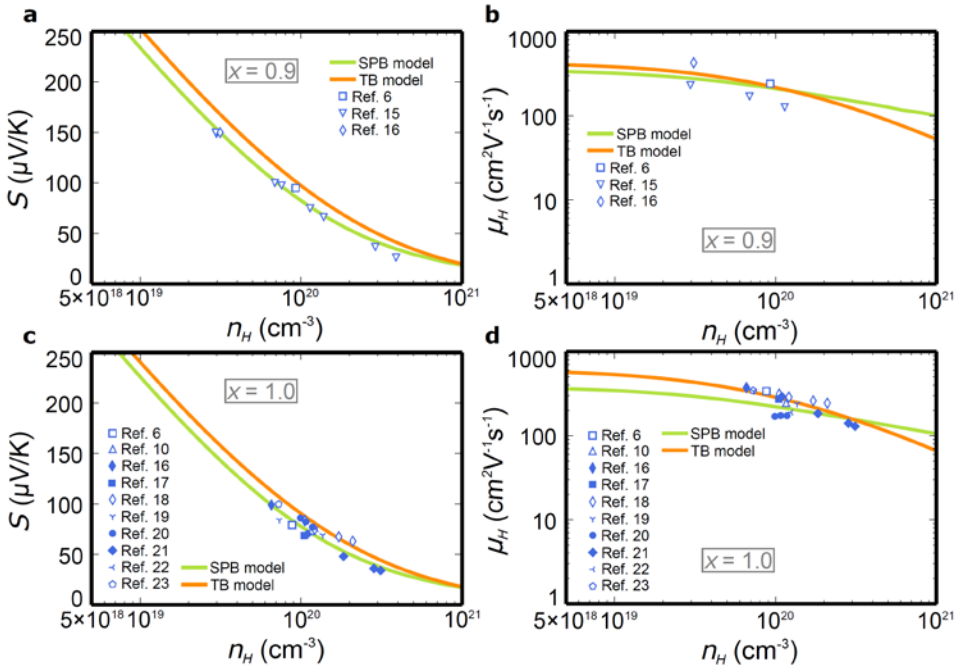

Fig. S6. Transport properties as a function of Hall carrier concentration (n_H) for $(Bi_{1-x}Sb_x)_2Te_3$ at 300 K. The Seebeck coefficient (S) and Hall mobility (μ_H) calculated by the TB model for x = 0.9 (*A*, *B*) and 1.0 (*C*, *D*) are shown in orange lines. The TB model was fitted to the literature data from Ref. [6, 10, 15-22], and Ref. [23] (empty shapes in blue). The result of SPB model (green line) was also plotted for comparison.

S5. References

[1] Y.I. Ravich, B.A. Efimova, I.A. Smirnov, Semiconducting Lead Chalcogenides, Plenum Press, New York, 1970.

[2] H. Wang, A.D. LaLonde, Y. Pei, G.J. Snyder, The Criteria for Beneficial Disorder in Thermoelectric Solid Solutions, Adv. Funct. Mater. 23(12) (2013) 1586-1596.

[3] E.H. Putley, Galvano- and thermo-magnetic coefficients for a multi-band conductor, Journal of Physics C: Solid State Physics 8(12) (1975) 1837.

[4] R. Sehr, L.R. Testardi, The optical properties of p-type Bi_2Te_3 - Sb_2Te_3 alloys between 2-15 microns, J. Phys. Chem. Solids 23(9) (1962) 1219-1224.

[5] Z.M. Gibbs, A. LaLonde, G.J. Snyder, Optical band gap and the Burstein–Moss effect in iodine doped PbTe using diffuse reflectance infrared Fourier transform spectroscopy, New Journal of Physics 15(7) (2013) 075020.

[6] M. Stordeur, M. Stölzer, H. Sobotta, V. Riede, Investigation of the Valence Band Structure of Thermoelectric $(Bi_{1-x}Sb_x)_2Te_3$ Single Crystals, Phys. Status Solidi B 150(1) (1988) 165-176.

[7] S. Walia, R. Weber, S. Sriram, M. Bhaskaran, K. Latham, S. Zhuiykov, K. Kalantar-zadeh, Sb_2Te_3 and Bi_2Te_3 based thermopower wave sources, Energ. Environ. Sci. 4(9) (2011) 3558-3564.

[8] F. Yang, T. Ikeda, G.J. Snyder, C. Dames, Effective thermal conductivity of polycrystalline materials with randomly oriented superlattice grains, J. Appl. Phys. 108(3) (2010) -.

[9] M. Stordeur, W. Kuhnberger, Nichtparabolizitat des Valenzbandes von Bi_2Te_3 gegolgert adu Transporteigenschaften, Phys. Status Solidi B 69 (1975) 377.

[10] L.R. Testardi, J.N. Bierly Jr, F.J. Donahoe, Transport properties of p-type Bi_2Te_3-Sb_2Te_3 alloys in the temperature range 80–370K, J. Phys. Chem. Solids 23(9) (1962) 1209-1217.

[11] H.-W. Jeon, H.-P. Ha, D.-B. Hyun, J.-D. Shim, Electrical and thermoelectrical properties of undoped Bi_2Te_3-Sb_2Te_3 and Bi_2Te_3-Sb_2Te_3-Sb_2Se_3 single crystals, J. Phys. Chem. Solids 52(4) (1991) 579-585.

[12] T. Plecháček, J. Navrátil, J. Horák, P. Lošťák, Defect structure of Pb-doped Bi_2Te_3 single crystals, Philos. Mag. 84(21) (2004) 2217-2228.

[13] M.K. Zhitinskaya, S.A. Nemov, T.E. Svechnikova, Specific features of Bi_2Te_3 doping with Sn, Phys. Solid State 40(8) (1998) 1297-1300.

[14] R.S. Erofeev, V.N. Ovechkina, Energy Spectrum of Solid Solutions of Bi_2Te_3-Sb_2Te_3 System, Izv. Akad. Nauk SSSR, Neorg. Mater. 17(10) (1981) 1780-1784.

[15] V.S. Gaidukova, R.S. Erofeev, V.N. Ovechkina, Characteristics of the energy spectrum of solid solutions in the SbTe-BiTe system, Izv. Akad. Nauk SSSR, Neorg. Mater. 17(2) (1981) 244 - 247.

[16] J. Jiang, L. Chen, S. Bai, Q. Yao, Q. Wang, Thermoelectric properties of p-type $(Bi_2Te_3)_x(Sb_2Te_3)_{1-x}$ crystals prepared via zone melting, J. Cryst. Growth 277(1–4) (2005) 258-263.

[17] M. Stordeur, G. Simon, Investigation of the Weak-Field Charge Transport in Semiconducting V2−VI3 Compounds with Trigonal Symmetry II. Interpretation of the Weak-Field Charge Transport in Sb_2Te_3 Single Crystals, Phys. Status Solidi B 124(2) (1984) 799-806.

[18] S. Scherrer, H. Scherrer, Bismuth Telluride, Antimony Telluride, and Their Solid Solutions, in: D.M. Rowe (Ed.), CRC Handbook of Thermoelectrics, CRC Press, Boca Raton, 1995.
[19] H.T. Langhammer, M. Stordeur, H. Sobotta, V. Riede, Optical and Electrical Investigations of the Anisotropy of Sb_2Te_3 Single Crystals, Phys. Status Solidi B 109(2) (1982) 673-681.
[20] J. Horák, L. Tichý, A. Vaško, M. Frumar, Reflectivity of iodine-doped Sb_2Te_3 crystals, Phys. Status Solidi A 14(1) (1972) 289-298.
[21] J. Horák, P. Lošťák, L. Šiška, M. Stordeur, The nature of silver impurity atoms in antimony telluride, Phys. Status Solidi B 114(1) (1982) 39-45.
[22] L. Tichý, J. Horák, A. Vaško, M. Frumar, Electrical properties of germanium-doped Sb_2Te_3 crystals, Phys. Status Solidi A 20(2) (1973) 717-724.
[23] V.A. Kulbachinskii, A.V.G. Kytin, P.M. Tarasov, Fermi surface and thermoelectric power of $(Bi_{1-x}Sb_x)_2Te_3$ single crystals doped by Ag, Sn, Ga, Thermoelectrics, 2006. ICT '06. 25th International Conference on, 2006, pp. 459-464.